Published in final edited form as:
Opt Lett. 2013 November 1; 38(21): 4374–4377.

Path-length-multiplexed scattering-angle-diverse optical coherence tomography for retinal imaging

Bingqing Wang[1,*], **Biwei Yin**[2], **Jordan Dwelle**[1], **H. Grady Rylander, III**[1], **Mia K. Markey**[1], and **Thomas E. Milner**[1]

[1]Department of Biomedical Engineering, The University of Texas at Austin, Austin, Texas 78712, USA

[2]Department of Electrical and Computer Engineering, The University of Texas at Austin, Austin, Texas 78712, USA

Abstract

A low-resolution path-length-multiplexed scattering angle diverse optical coherence tomography (PM-SAD-OCT) is constructed to investigate the scattering properties of the retinal nerve fiber layer (RNFL). Low-resolution PM-SADOCT retinal images acquired from a healthy human subject show the variation of RNFL scattering properties at retinal locations around the optic nerve head. The results are consistent with known retinal ganglion cell neural anatomy and principles of light scattering. Application of PM-SAD-OCT may provide potentially valuable diagnostic information for clinical retinal imaging.

Optical coherence tomography (OCT) is routinely used by ophthalmologists to record diagnostic retinal images. Important features in recorded OCT retinal images include structural integrity and retinal nerve fiber layer (RNFL) thickness for glaucoma diagnostics [1]. In addition, the optical scattering properties of RNFL may provide diagnostic information. Changes of optical scattering properties in cells undergoing apoptosis, largely due to intensified mitochondrial fission, have been observed in a number of studies. Using a Fourier microscopy instrument, Pasternack *et al.* found that early cell apoptosis is accompanied by mitochondrial fission, which results in more isotropic or large-angle light scattering [2]. Chalut *et al.* presented an angle-resolved low-coherence interferometry system to measure scattering changes of cells in early apoptotic stages, which the authors suggested may involve mitochondrial fission [3]. Recently, Ju *et al.* reported that mitochondrial fission in differentiated retinal ganglion cell (RGC) cultures is induced in response to a glaucoma-like environment of elevated hydrostatic pressure [4]. The observed structural changes in mitochondrial networks associated with some neurological diseases suggest that angular scattering properties of RNFL may provide diagnostic information for retinal diseases like glaucoma.

Recent studies suggest that the change of RNFL scattering properties in glaucomatous eyes results in decreased RNFL reflectance, which was found to be a sensitive, robust, and early diagnostic glaucoma indicator. For example, Dwelle *et al.* investigated RNFL thickness, phase retardation, birefringence and other parameters and found that the earliest change associated with elevated intraocular pressure (IOP) in glaucomatous eyes of nonhuman primates is decreased RNFL reflectance [5]. Liu *et al.* compared the performance of multiple glaucoma diagnostic indicators and identified RNFL reflectance as the best indicator to

[*]Corresponding author: bingqing.wang@utexas.edu.

distinguish between control and glaucoma eyes and control and glaucoma-suspect eyes [6]. Huang *et al.* observed decreased RNFL reflectance prior to decreased thickness in glaucomatous retinas [7]. These observations suggest that measurement of RNFL scattering properties during retinal imaging may provide a valuable and early diagnostic indicator of glaucoma.

Pyhtila *et al.* [8] and Wax *et al.* [9] first reported the application of an angle-resolved spectral domain OCT system to characterize the size of Mie scattering centers. Iftimia *et al.* reported a time-domain OCT system using path-length-encoded angular compounding for speckle reduction [10]. Later, various angle-resolved OCT designs were reported for speckle reduction [11–13], light-scattering spectroscopy [14], focus extension [15], and measurement of absolute flow velocities [16–19]. In particular, Klein *et al.* acquired angle-resolved OCT images from human retina for speckle reduction purposes and mentioned the possibility of using angle-resolved OCT to achieve tissue discrimination [13]. The authors are not aware of any published studies that report an angle diverse OCT system to measure RNFL angular scattering properties. In this Letter, we present a low-resolution path-length-multiplexed scattering-angle-diverse OCT (PM-SAD-OCT) approach that is capable of measuring spatial variation in the angular distribution of RNFL backscattered light in retinal images.

The PM-SAD-OCT imaging system reported here is based on a swept-source ophthalmologic OCT imaging system described previously at 1060 ± 30 nm wavelength that records 28,000 A-scans per second [20]. PM-SAD-OCT uses path-length multiplexing to separate incident and backscattered light from the retina into discrete angular ranges by placing a path-length multiplexing element (PME) in the sample path of the interferometer between the collimating lens and scanning mirrors close to the conjugate position of the patient's pupil. The PME is constructed of a t = 3.0 mm thick BK7 glass window with a 2.0 mm diameter clear aperture in the center (Fig. 1). Light propagating through the central region of the PME (Region-1) has a short path with an optical thickness $n_{air}t$ = 3.0 mm, where n_{air} = 1 is the refractive index of air. Light propagating through the outer region (Region-2) has a long path and consists of a BK7 glass annular aperture with optical thickness $n_{glass}t$ = 4.52 mm, where n_{glass} = 1.50669 is the refractive index of BK7 glass at λ = 1060 nm.

The composite optical path-length of detected light returned from the RNFL is dependent on position of incoming or returning light in the patient's pupil and is associated with the angle of light incident to or backscattered from the RNFL. The diameter of the central clear aperture (2.0 mm) is smaller than the $1/e^2$ diameter (6.0 mm) of the sample beam. Optical path-lengths of four incident-backscattered light paths through the PME are recognized (Fig. 2): (1) *short–short*, in which light incident on the patient's pupil propagates through Region-1 (low angle), backscatters from the RNFL at a low angle, and returns through Region-1 with a relative composite path-length of $2n_{air}t$; (2) *short–long*, in which light propagates through Region-1 (low angle), backscatters at a high angle from the RNFL, and returns through Region-2 with a relative composite path-length of $n_{air}t + n_{glass}t$; (3) *long–short*, in which light propagates through Region-2 (high angle), backscatters at a low angle from the RNFL and returns through Region-1 with a relative composite path-length of $n_{glass}t + n_{air}t$; and (4) long– long, in which light propagates through Region-2 (high angle), backscatters from the RNFL, and returns through Region-2 with a relative composite path-length of $2n_{glass}t$. Optical path-lengths of *short–long* and *long–short* paths are degenerate. As a result, PM-SAD-OCT data consists of *three* retinal subimages (Fig. 3A, Table 1) separated by $(n_{glass}\text{-}n_{air})t$ = 1.52007 mm.

The amplitude of PM-SAD-OCT signal, or pixel brightness in PM-SAD-OCT subimages, is proportional to the square root of scattered light intensity collected from the sample ($\sqrt{I_s}$). However, pixel brightness in PM-SAD-OCT images is also affected by decay of the swept-source coherence function $\Gamma(n_g c\,\tau)$ with increasing scan depth ($n_g c\,\tau$), where n_g is the group refractive index of the retina, c is the speed of light in vacuum, and τ is the round-trip time delay between light in the sample and reference paths. As a result, the PM-SAD-OCT subimage with longer optical path-length has a decreased brightness since the amplitude of the OCT point-spread function decreases with increasing depth. To determine the relative angular distribution of RNFL backscattered light in PM-SAD-OCT subimages, PM-SAD-OCT subimages are normalized by the experimentally measured depth-dependent amplitude of the OCT autocorrelation function.

To demonstrate the feasibility of PM-SAD-OCT to measure spatial variation of the RNFL backscattering properties, retinal ring scans were collected in a dimly lit room from five healthy subjects' right eyes (age between 24 and 30) without pharmacological dilation (Fig. 3). Three PM-SAD-OCT retinal subimages are observed as expected (Fig. 3A). The low-to-high angle RNFL backscattering anisotropy was defined to examine the spatial variation of RNFL scattering properties by $I_{\mathrm{Low}}/I_{\mathrm{High}}$where I_{Low} and I_{High} are the average RNFL intensity in the low-angle and high-angle subimages, respectively. To study the peripapillary variation of RNFL scattering properties, a retinal scan with 10 peripapillary ring scans centered on the optic nerve head (ONH) with diameters ranging from 1.25 to 4.44 mm was performed. After correcting for the depth-dependent OCT autocorrelation function and segmenting RNFL from each subimage, $I_{\mathrm{Low}}/I_{\mathrm{High}}$ was computed in the RNFL for each of the 10 peripapillary ring scans and plotted over the retinal area imaged (Fig. 3B). $I_{\mathrm{Low}}/I_{\mathrm{High}}$ was averaged over the 10 ring scans to give the peripapillary variation around the ONH (Fig. 3C). For all five subjects, $I_{\mathrm{Low}}/I_{\mathrm{High}}$ is smallest (largest) in the temporal (nasal) quadrant. PM-SAD-OCT results suggest that for all five healthy human subjects, RGC axonal scattering structures (e.g., microtubules, cell membranes, and mitochondria networks) in the temporal (nasal) quadrant backscatter incident light at relatively larger (smaller) angles compared to those structures in the superior and inferior quadrants. RGC axons in normal human subjects are known to have the smallest diameter in the temporal quadrant [21], so the angle of RNFL backscattered light in this region is expected to be larger and is consistent with $I_{\mathrm{Low}}/I_{\mathrm{High}}$ determined from PM-SAD-OCT. Moreover, $I_{\mathrm{Low}}/I_{\mathrm{High}}$ shows a similar trend with relative axoplasmic area, defined as the difference between axon area and the total organelle area for each RGC axon, around the ONH measured from primate eyes [22] (Fig. 3D).

As mentioned above, the measurement from PM-SAD-OCT is low-to-high angle RNFL backscattering anisotropy, defined as the intensity ratio of low-angle and high-angle backscattering ($I_{\mathrm{Low}}/I_{\mathrm{High}}$). Repeatability of $I_{\mathrm{Low}}/I_{\mathrm{High}}$ was measured by recording four successive peripapillary ring scans with an average scan-to-scan variation of less than 7%.

The dependency of $I_{\mathrm{Low}}/I_{\mathrm{High}}$ on incident light polarization and angle between incident light and sample normal was investigated. The polarization state of light incident on the cornea was varied with a broadband bulk electro-optic modulator described previously [20]. For a retinal ring scan, three A-scans were recorded with different incident polarization states (separated by 120° on the great circle in the Q–U plane on the Poincaré sphere). $I_{\mathrm{Low}}/I_{\mathrm{High}}$ was independent of the three incident polarization states.

An RNFL phantom [20, 23] was utilized to investigate the dependence of $I_{\mathrm{Low}}/I_{\mathrm{High}}$ on the relative angle between incident light and the sample surface normal. The RNFL phantom was positioned under the PM-SAD-OCT beam and tilted from the normal over a 23° angular range. Point measurement without scanning was performed and $I_{\mathrm{Low}}/I_{\mathrm{High}}$ was calculated at

each tilt angle. I_{Low}/I_{High} was found to be dependent on the angle between incident light and the RNFL phantom surface normal. At angles larger than the numerical aperture angle of incident light, I_{Low}/I_{High} decreases monotonically with increasing angle.

Since the ring scan around the ONH is an off-axis measurement, for the largest radius (2.22 mm) retinal scan about the ONH, the angle between incident light and RNFL normal varies from about 7° (temporal quadrant) to 22° (nasal quadrant). Considering that the numerical aperture angle of the OCT beam incident on the RNFL is less than 2.53°, the angle between incident light and RNFL normal in the above measurement is more than 3× greater than the numerical aperture angle at all retinal positions. According to results from the RNFL phantom study, variation of the angle between incident light and RNFL normal is expected to increase the value of I_{Low}/I_{High} in the temporal quadrant and decrease I_{Low}/I_{High} in the nasal quadrant. However, the measured I_{Low}/I_{High} was lowest in the temporal and highest in the nasal quadrant. Therefore, we think the observed variation in the ratio I_{Low}/I_{High} is due, at least in part, to structural variation of the RNFL. If the angular scattering properties of the RNFL phantom are substantially different from those of the nerve fibers, then the angle of the nerve fiber layer with respect to the incident light could impact the measurements.

I_{Low}/I_{High} is calculated based on OCT image intensity, which is affected by speckle noise. Thicker RNFL provides more image pixels to average and calculate I_{Low} and $I_{High}$and as a result gives a more accurate calculation of I_{Low}/I_{High} in terms of signal-to-noise ratio. To minimize the accuracy problems from speckle noise, we averaged 40 B-scans at the same location at each of the 10 rings around the ONH. By performing sufficient averaging, the noise level is fairly low so that RNFL thickness does not affect the accuracy of I_{Low}/I_{High}. On the other hand, a thicker RNFL introduces more scattering events and can broaden backscattering angular distribution, potentially making the calculation of I_{Low}/I_{High} less reliable in terms of representing tissue scattering properties.

The hypothesis underlying the application of PM-SADOCT is that the scattering properties of some tissues (e.g., RNFL) may change in early-stage diseases (e.g., glaucoma). Although scattering changes have been observed in both nonhuman primate and human eyes [5, 6], more studies are necessary to document the origins of the change of RNFL scattering properties.

While the PM-SAD-OCT reported here is promising for characterizing retinal scattering properties that may be relevant for early-stage glaucoma diagnosis, a number of limitations are recognized. First, the incident light is not constrained to a single incident direction, which has the effect of blurring angle-resolved data. Second, the current configuration of PM-SAD-OCT reported here has limited angular resolution with only three discrete subimages, and higher angular resolution might enhance some applications. The number of PM-SAD-OCT subimages can be increased, at the cost of reduced signal strength in each subimage and a requirement for a light source having increased coherence length. Third, the angular range (2.53°, Fig. 2) in the current configuration is fairly small compared to previous nonophthalmological studies [8, 9, 11, 12, 14]. The small angular range limits the utility of the instrument in terms of detecting scattering changes in a sample. A larger angular range is expected to improve system sensitivity to detect variations in sample scattering properties. On the other hand, even with a limited angular range and low angular resolution, a spatial variation in the backscattered RNFL light signal is observed.

In summary, low-resolution PM-SAD-OCT images from healthy human retinas suggest that, for the recorded scans, RGC axonal structures in the temporal (nasal) quadrant backscatter light at larger (smaller) angles compared to superior and inferior quadrants. The results are consistent with known RGC neural anatomy and principles of light scattering. This is the

first report, to the best of our knowledge, that suggests angular resolved OCT approaches can provide additional information on the scattering properties of the RNFL and may provide value for detection of conditions that are associated with cellular level morphology.

References

1. Schuman JS, Hee MR, Puliafito CA, Wong C, Pedut-Kloizman T, Lin CP, Hertzmark E, Izatt JA, Swanson EA, Fujimoto JG. Arch. Ophthalmol. 1995; 113:586. [PubMed: 7748128]
2. Pasternack RM, Zheng J, Boustany NN. Cytom. A. 2011; 79A:137.
3. Chalut KJ, Ostrander JH, Giacomelli MG, Wax A. Cancer Res. 2009; 69:1199. [PubMed: 19141640]
4. Ju W, Liu Q, Kim K, Crowston JG, Lindsey JD, Agarwal N, Ellisman MH, Perkins GA, Weinreb RN. Invest. Ophthalmol. Vis. Sci. 2007; 48:2145. [PubMed: 17460273]
5. Dwelle J, Liu S, Wang B, McElroy A, Ho D, Markey MK, Milner T, Rylander HG III. Invest. Ophthalmol. Vis. Sci. 2012; 53:4380. [PubMed: 22570345]
6. Liu S, Wang B, Yin B, Milner TE, Markey MK, McKinnon SJ, Rylander HG III. Retinal nerve fiber layer reflectance for early glaucoma diagnosis. J. Glaucoma. (to be published).
7. Huang X, Zhou Y, Kong W, Knighton RW. Investig. Ophthalmol. Vis. Sci. 2011; 52:6737. [PubMed: 21730345]
8. Pyhtila JW, Graf RN, Wax A. Optics Express. 2003; 11:3473. [PubMed: 19471481]
9. Wax A, Yang C, Backman V, Badizadegan K, Boone CW, Dasari RR, Feld MS. Biophys. J. 2002; 82:2256. [PubMed: 11916880]
10. Iftimia N, Bouma BE, Tearney GJ. J. Biomed. Opt. 2003; 8:260. [PubMed: 12683852]
11. Desjardins AE, Vakoc BJ, Oh WY, Motaghiannezam SMR, Tearney GJ, Bouma BE. Opt. Express. 2007; 15:6200. [PubMed: 19546925]
12. Desjardins AE, Vakoc BJ, Tearney GJ, Bouma BE. Opt. Express. 2006; 14:4736. [PubMed: 19516630]
13. Klein T, André R, Wieser W, Pfeiffer T, Huber R. Biomed. Opt. Express. 2013; 4:619. [PubMed: 23577296]
14. Pyhtila JW, Boyer JD, Chalut KJ, Wax A. Opt. Lett. 2006; 31:772. [PubMed: 16544619]
15. Mo J, de Groot M, de Boer JF. Opt. Express. 2013; 21:10048. [PubMed: 23609710]
16. Werkmeister RM, Dragostinoff N, Pircher M, Götzinger E, Hitzenberger CK, Leitgeb RA, Schmetterer L. Opt. Lett. 2008; 33:2967. [PubMed: 19079508]
17. Zotter S, Pircher M, Torzicky T, Bonesi M, Götzinger E, Leitgeb RA, Hitzenberger CK. Opt. Express. 2011; 19:1217. [PubMed: 21263663]
18. Pedersen CJ, Huang D, Shure MA, Rollins AM. Opt. Lett. 2007; 32:506. [PubMed: 17392903]
19. Makita S, Jaillon F, Yamanari M, Miura M, Yasuno Y. Opt. Express. 2011; 19:1271. [PubMed: 21263668]
20. Elmaanaoui B, Wang B, Dwelle JC, McElroy AB, Liu SS, Rylander HG, Milner TE. Opt. Express. 2011; 19:10252. [PubMed: 21643283]
21. Hildebrand, GD.; Fielder, AR. Anatomy and Physiology of the Retina. Springer; 2011. p. 39-65.
22. Pocock GM, Aranibar RG, Kemp NJ, Specht CS, Markey MK, Rylander HG. Investig. Ophthalmol. Vis. Sci. 2009; 50:5238. [PubMed: 19494208]
23. Kemp NJ, Park J, Zaatari HN, Rylander HG, Milner TE. J. Opt. Soc. Am. A. 2005; 22:552.

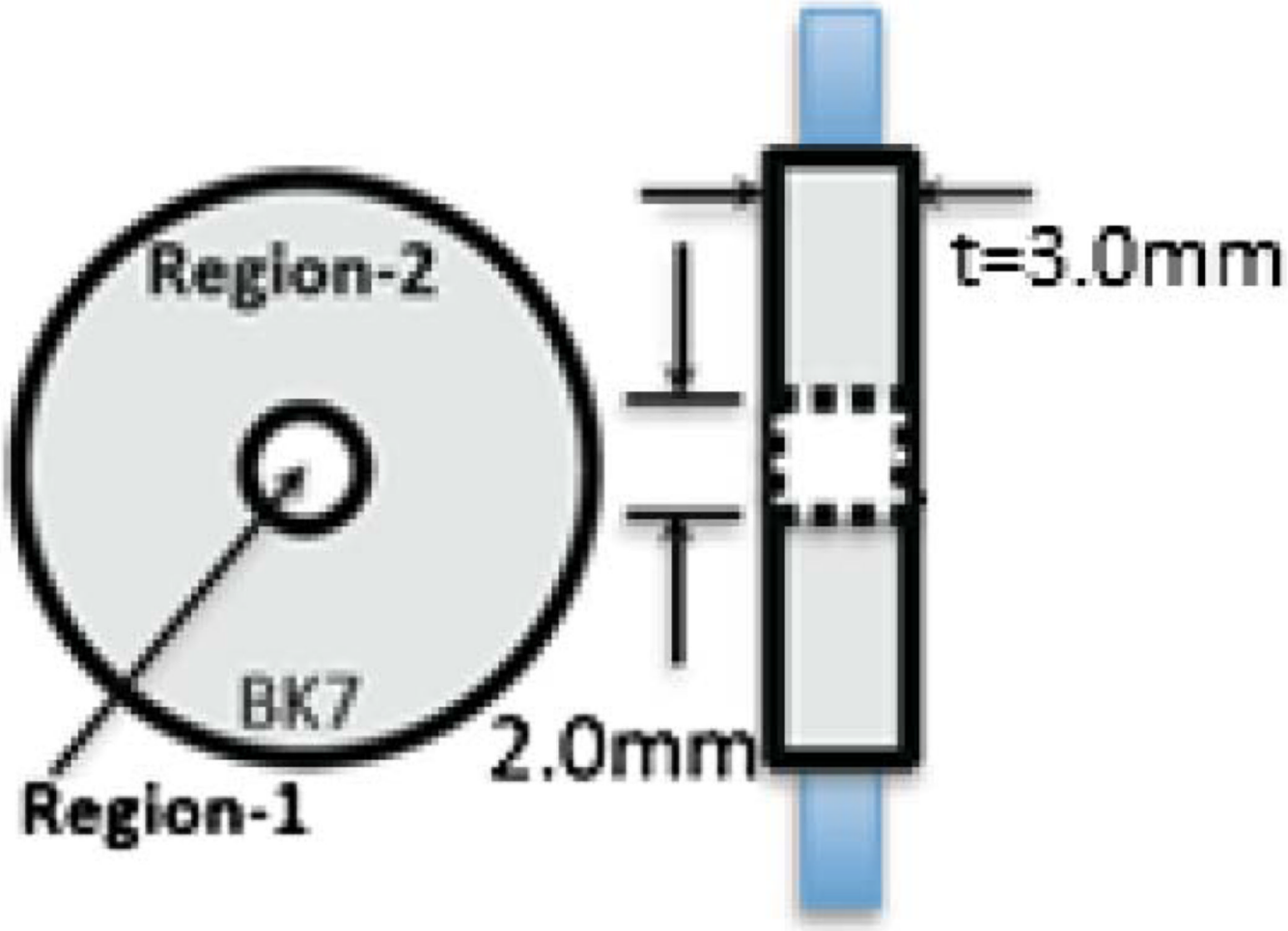

Fig. 1.
PME constructed of 3.0 mm thick BK7 glass window. Region-1 is the inner 2.0 mm diameter aperture. Region-2 is the outer annulus. Left, end-on view; right, side view.

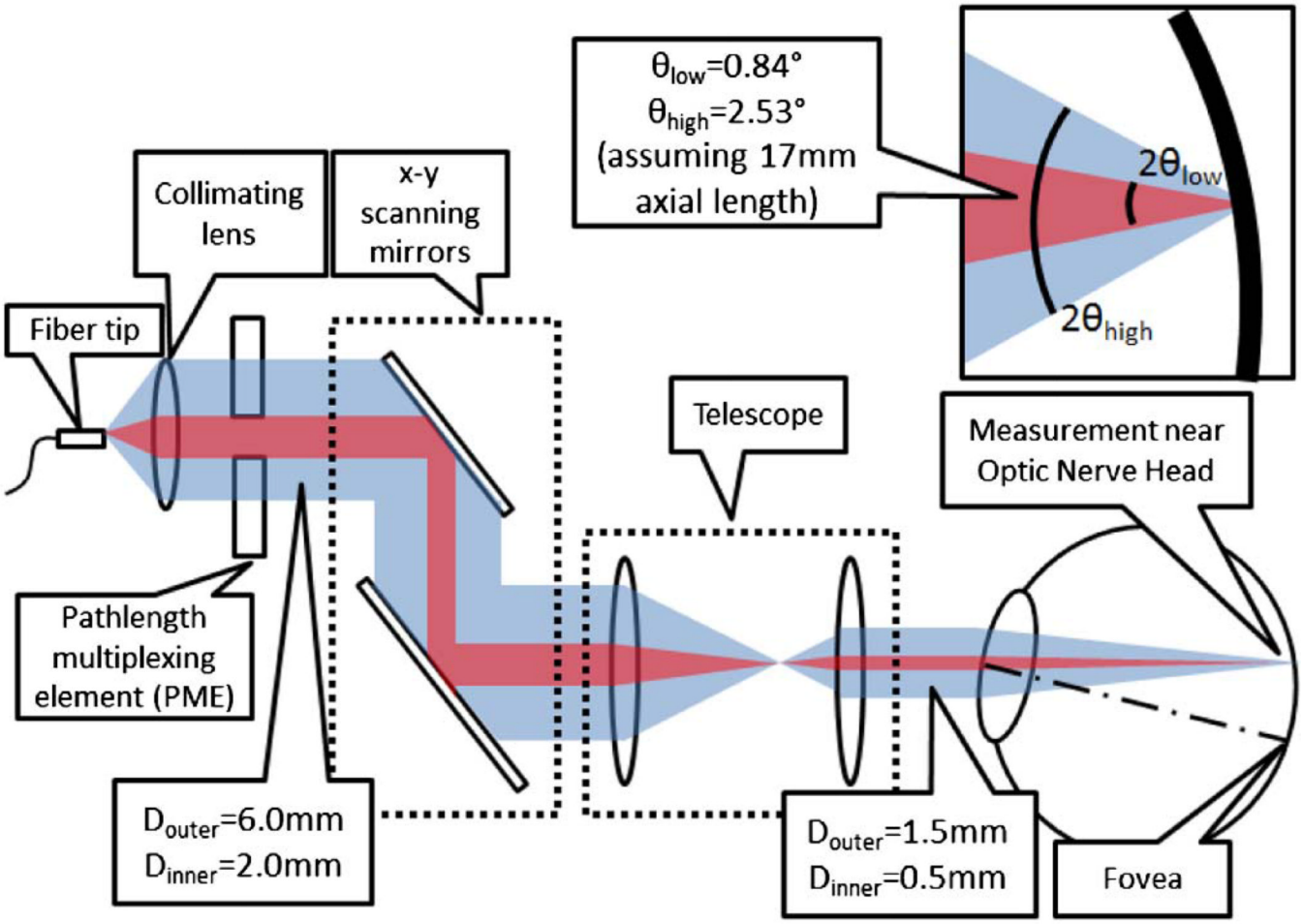

Fig. 2.
PME is positioned in the sample path of the interferometer. Low-angle (short–short, red) and high-angle (long–long, blue) backscattered RNFL light paths are shown.

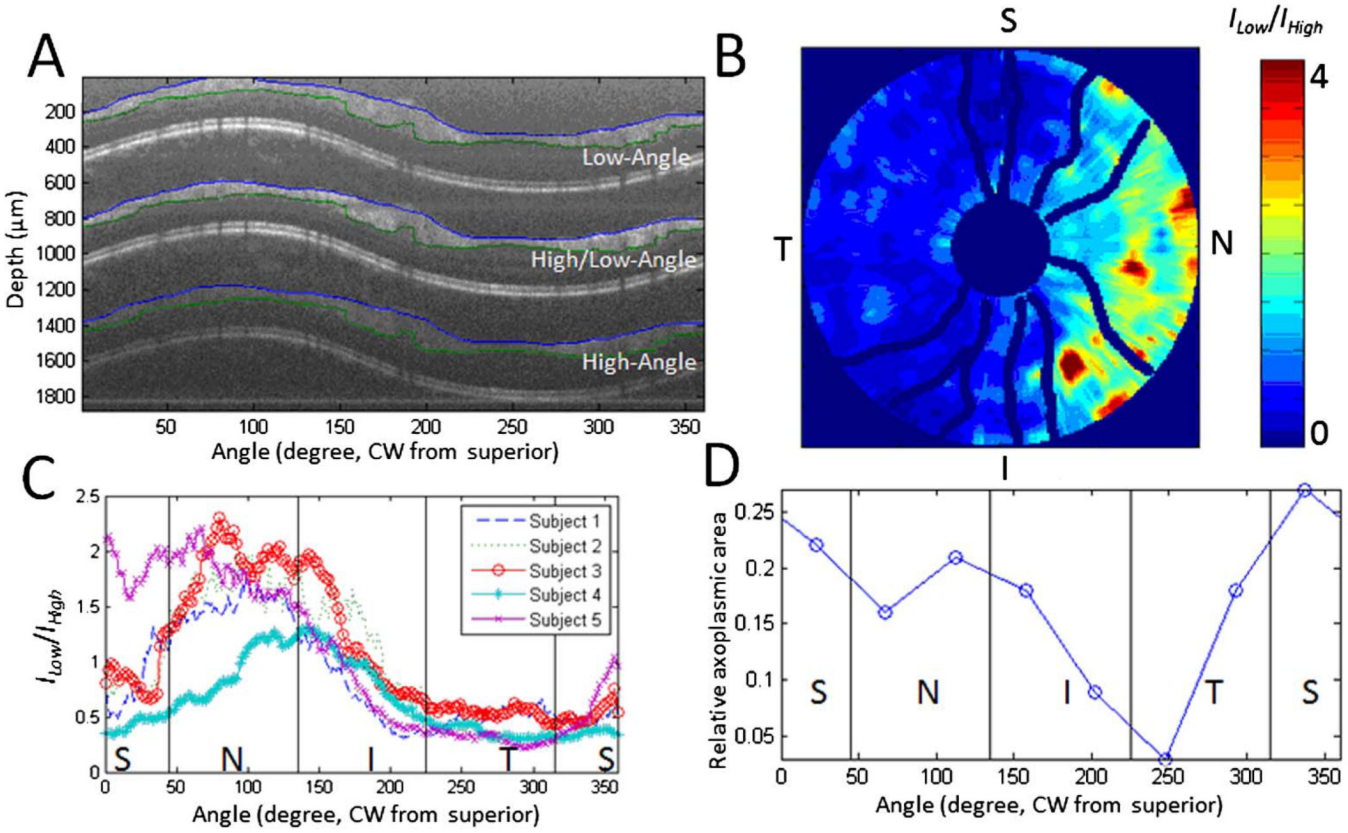

Fig. 3.

A, PM-SAD-OCT retinal subimages of a healthy human subject correspond to low-angle (upper), high/low-angle (middle), and high-angle (lower) images collected from to a 4.4 mm diameter ring scan. Segmentation of RNFL in each subimage is indicated by blue and green lines. B, Retinal map of low-to-high angle RNFL backscattering anisotropy (I_{Low}/I_{High}) by recording 10 peripapillary ring scans centered on the ONH with diameters ranging from 1.25 to 4.44 mm. Blood vessels are shown with dark blue lines. C, Peripapillary variation of averaged I_{Low}/I_{High} of five healthy subjects. D, Peripapillary variation of averaged relative axoplasmic mode around the ONH measured from a nonhuman primate's eye.

Table 1

Properties of Three PM-SAD-OCT Subimages

	Incident-Collected Path	Relative Composite Path-length	Incident-Scattered Angle	Possible Scattering Angle Range	Averaged Scattering Angle
Upper subimage	Short–short	$2n_{air}t$	Low–low	$[0, 2\theta_{low}]$	Low
Middle subimage	Short–long or Long–short	$n_{air}t + n_{glass}t$	Low–high or High–low	$[0, \theta_{low} + \theta_{high}]$	Higher
Lower subimage	Long–long	$2n_{glass}t$	High–high	$[0, 2\theta_{high}]$	Highest